MUSIC-characterization of small scatterers for normal measurement data

2009 Inverse Problems 25 075012

(http://iopscience.iop.org/0266-5611/25/7/075012)

IOP PUBLISHING INVERSE PROBLEMS

Inverse Problems **25** (2009) 075012 (12pp) doi:10.1088/0266-5611/25/7/075012

MUSIC-characterization of small scatterers for normal measurement data

Roland Griesmaier[1] **and Martin Hanke**[2]

[1] Department of Mathematical Sciences, University of Delaware, Newark, DE 19716, USA
[2] Institut für Mathematik, Johannes Gutenberg-Universität, 55099 Mainz, Germany

E-mail: griesmai@math.udel.edu and hanke@math.uni-mainz.de

Received 5 May 2009, in final form 22 May 2009
Published 18 June 2009
Online at stacks.iop.org/IP/25/075012

Abstract

We investigate the reconstruction of the positions of a collection of small metallic objects buried beneath the ground from measurements of the vertical component of scattered fields corresponding to vertically polarized dipole excitations on a horizontal two-dimensional measurement device above the surface of the ground. A MUSIC reconstruction method for this problem has recently been proposed by Iakovleva *et al* (2007 *IEEE Trans. Antennas Propag.* **55** 2598). In this paper, we give a rigorous theoretical justification of this method. To that end we prove a characterization of the positions of the scatterers in terms of the measurement data, applying an asymptotic analysis of the scattered fields. We present numerical results to illustrate our theoretical findings.

(Some figures in this article are in colour only in the electronic version)

1. Introduction

We investigate a MUSIC method to detect a collection of small metallic objects buried in the subsoil from near field measurements of time-harmonic electromagnetic fields above the surface of the ground. One possible application we have in mind is the detection of buried land mines using a multi-static measurement device that contains a grid of coils to excite and measure electromagnetic waves. Our assumption on the size of the scatterers is motivated by the fact that metal components contained in land mines are usually tiny (with diameters of few centimeters at most), while metal detectors for humanitarian demining often work at very low frequencies (cf [10]) corresponding to wavelengths in the order of kilometers.

As a simplified mathematical model we consider an unbounded two-layered background medium representing air and soil, respectively, with finitely many small perfectly conducting

scatterers buried in the soil, and an idealized measurement device operating above the ground. This device provides the sources for the incident fields and is measuring the corresponding scattered fields. The goal of the inverse problem is to recover the number and the positions of the unknown scatterers.

To this end we consider a MUSIC method. This is a non-iterative reconstruction algorithm for inverse scattering problems that is particularly adapted to the reconstruction of small or point-like scatterers, and has proved to be comparatively robust, even in the presence of noisy data. Starting with the work by Devaney [16], MUSIC methods have been studied by various authors, e.g., in [2–5, 8, 9, 12, 18–21, 23]. Following Brühl *et al* [9], a rigorous foundation of these methods can be based on an asymptotic analysis of the scattered fields as the size of the scatterers tends to zero. It turns out that the leading order term in the asymptotic expansion of the scattered fields is a superposition of dipole fields with singularities at the positions of the scatterers. This enables the development of a binary criterion to decide whether a given point in the region of interest supports such an infinitesimal scatterer or not—using only the measured data as input. An excellent introduction into this field can be found in the books by Ammari and Kang [6, 7].

We mention that similar arguments can be used to justify so-called factorization methods and linear sampling methods for the reconstruction of the full shape of objects of arbitrary (not necessarily small) size from scattering data (cf, e.g., [11, 24] for surveys on these methods). The relation between these methods and the MUSIC methods has been pointed out in [1, 12, 19, 23].

The asymptotic analysis of the electromagnetic scattering problem of infinitesimal scatterers in two-layered background media, i.e., the direct problem, has been carried out in [19]. In this paper one can also find a MUSIC method for a corresponding inverse problem, using the full three-dimensional traces of the scattered magnetic fields as data, for every possible (vector valued) magnetic source supported on this device.

From a practical point of view, however, it is desirable to reduce this large amount of measured data. For example, Iakovleva *et al* [21] have recently presented a MUSIC method for a modification of the above inverse problem, which only uses

(i) incident fields whose polarization is perpendicular to the device;
(ii) measurements of the normal component of the scattered fields.

This setup mimicks a multi-static measurement device of several coils that are mounted parallel to the surface of ground.

In this work we provide a theoretical foundation of the method from [21], and we prove that the positions of the infinitesimal scatterers can be recovered from the given normal measurement data. Although we can utilize the asymptotic analysis from [19] of the forward problem to achieve our goal, the techniques from [19] for treating the inverse problem considered there break down for the particular setting of [21]. We therefore need to develop a somewhat different line of argument instead. Our findings nicely support and complement the results from [21], in particular those concerning the structure of the singular value decomposition of the associated multi-static response matrix.

The outline of this paper is as follows. In section 2, we describe the mathematical model for the scattering and measurement process we are going to use and summarize the results of the asymptotic analysis from [19]. Then we develop the theoretical foundation of the MUSIC method for normal excitations and measurements in section 3. Finally, in section 4, we formulate the reconstruction algorithm and provide numerical examples to further illustrate the performance of this method. We also compare these results to numerical results from [19, 20], which utilize fully three-dimensional excitations and measurements.

2. The direct scattering problem

The mathematical setting of our direct scattering problem is the same as in [19, 20]: we consider a two-layered medium $\mathbb{R}^3 = \mathbb{R}^3_+ \cup \Sigma_0 \cup \mathbb{R}^3_-$, where $\Sigma_0 := \{\boldsymbol{x} \in \mathbb{R}^3 \mid x_3 = 0\}$ corresponds to the surface of ground and the two half spaces $\mathbb{R}^3_+$ and $\mathbb{R}^3_-$ above and below Σ_0 represent air and soil, respectively. Both half spaces are assumed to be filled with homogeneous isotropic materials such that the electric permittivity ε and the magnetic permeability μ are given by

$$\varepsilon(\boldsymbol{x}) := \begin{cases} \varepsilon_+, & \boldsymbol{x} \in \mathbb{R}^3_+, \\ \varepsilon_-, & \boldsymbol{x} \in \mathbb{R}^3_-, \end{cases} \qquad \mu(\boldsymbol{x}) := \begin{cases} \mu_+, & \boldsymbol{x} \in \mathbb{R}^3_+, \\ \mu_-, & \boldsymbol{x} \in \mathbb{R}^3_-, \end{cases}$$

where ε_+ and $\mu_\pm$ are positive, whereas ε_- may be complex with $\mathrm{Re}(\varepsilon_-) > 0$ and $\mathrm{Im}(\varepsilon_-) \geqslant 0$ to allow for conductive soils.

Throughout we study time-harmonic electromagnetic waves with an angular velocity $\omega > 0$, which are governed by the reduced Maxwell equations

$$\mathbf{curl}\, \boldsymbol{H} + \mathrm{i}\omega\varepsilon \boldsymbol{E} = 0, \quad \mathbf{curl}\, \boldsymbol{E} - \mathrm{i}\,\omega\mu \boldsymbol{H} = 0. \tag{1}$$

The associated (discontinuous) wave number is

$$k := \omega\sqrt{\varepsilon\mu} = \begin{cases} k_+, & \boldsymbol{x} \in \mathbb{R}^3_+, \\ k_-, & \boldsymbol{x} \in \mathbb{R}^3_-, \end{cases}$$

with $k_+ \in \mathbb{R}$, $k_+ > 0$, and $\mathrm{Im}(k_-) \geqslant 0$. Solutions to (1) satisfying the Silver–Müller radiation condition

$$\int_{\partial B_R} \left| \frac{\boldsymbol{x}}{R} \times \boldsymbol{H}(\boldsymbol{x}) + \left(\frac{\varepsilon(\boldsymbol{x})}{\mu(\boldsymbol{x})}\right)^{1/2} \boldsymbol{E}(\boldsymbol{x}) \right|^2 \mathrm{d}s(\boldsymbol{x}) = o(1) \qquad \text{as} \quad R \to \infty, \tag{2}$$

where B_R denotes the ball of radius R around the origin, are called radiating solutions.

We suppose that a finite collection of small perfectly conducting objects is buried in the lower half space. Each of these scatterers is assumed to have the form $D_{\delta,l} := \boldsymbol{z}_l + \delta B_l$, $1 \leqslant l \leqslant p$, where $\boldsymbol{z}_l \neq \boldsymbol{z}_j$ for $l \neq j$ and $B_l \subset \mathbb{R}^3$ is a bounded simply connected domain with a smooth, connected boundary. We refer to $\boldsymbol{z}_l \in \mathbb{R}^3_-$ as the *position* of the scatterer $D_{\delta,l}$, and to the value of $\delta > 0$ as its *size*. We assume δ to be small enough such that the individual scatterers do not overlap. The union of all scatterers is denoted by $D_\delta := \bigcup_{l=1}^p D_{\delta,l}$.

The scattering of an incident wave $(\boldsymbol{E}^i, \boldsymbol{H}^i)$ by these objects is modeled by an exterior boundary value problem for Maxwell's equations (1) in $\mathbb{R}^3 \backslash \overline{D_\delta}$ for the scattered wave $(\boldsymbol{E}^s, \boldsymbol{H}^s)$ subject to the boundary condition $\boldsymbol{\nu} \times \boldsymbol{E}^s|_{\partial D_\delta} = -\boldsymbol{\nu} \times \boldsymbol{E}^i|_{\partial D_\delta}$ and the Silver–Müller radiation condition (2) (see, e.g., Monk [27]).

In contrast to [19, 20] we restrict our attention to a constrained set of incident fields, namely magnetic fields that are generated by *vertically polarized* magnetic dipole distributions on a relatively open bounded domain $\mathcal{M} \subset \Sigma_d := \left\{\boldsymbol{x} \in \mathbb{R}^3_+ \,\middle|\, x_3 = d\right\}$ in the upper half space, i.e., for some fixed $d > 0$. We think of $\mathcal{M}$ as the location of a multi-static measurement device that consists of a sufficiently large number of coils in horizontal alignment: our numerical examples in section 4 allude to a setup with 36 coils.

The incident electromagnetic field can thus be written in $\mathbb{R}^3 \backslash \mathcal{M}$ as

$$\boldsymbol{H}^i := k_+^2 \int_{\mathcal{M}} \varphi(\boldsymbol{y}) \mathbb{G}^m(\cdot, \boldsymbol{y}) \boldsymbol{e}_3 \,\mathrm{d}s(\boldsymbol{y}), \qquad \boldsymbol{E}^i := -\frac{1}{\mathrm{i}\omega\varepsilon} \mathbf{curl}\, \boldsymbol{H}^i, \tag{3}$$

where $\varphi \in L^2(\mathcal{M}; \mathbb{C})$ is the (scalar valued) dipole density and $\boldsymbol{e}_3 := (0, 0, 1)^\top$ represents the vertical polarization of the magnetic dipoles. Here, $\mathbb{G}^m$ denotes the magnetic dyadic Green's function, i.e., the (distributional) solution of

$$\mathbf{curl}_x \frac{1}{\varepsilon(\boldsymbol{x})} \mathbf{curl}_x \mathbb{G}^m(\boldsymbol{x}, \boldsymbol{y}) - \omega^2 \mu(\boldsymbol{x}) \mathbb{G}^m(\boldsymbol{x}, \boldsymbol{y}) = \frac{1}{\varepsilon(\boldsymbol{x})} \delta(\boldsymbol{x} - \boldsymbol{y}) \mathbb{I}_3,$$

$\boldsymbol{x}, \boldsymbol{y} \in \mathbb{R}^3$, where $\mathbb{I}_3$ denotes the 3×3 identity matrix, together with appropriate Silver–Müller radiation conditions similar to (2). The electric dyadic Green's function $\mathbb{G}^e$ is defined by the same equations, but with ε and μ interchanged.

The other difference to the setting in [19, 20] concerns the measured quantities: while the full (3D) scattered fields are measured in [19, 20], here we only consider the normal trace of the magnetic field $\boldsymbol{H}^s$ on $\mathcal{M}$, in agreement with our modeling assumption that the coils are all mounted horizontally. Accordingly we introduce the measurement operator

$$G_{\delta,n} : L^2(\mathcal{M}; \mathbb{C}) \to L^2(\mathcal{M}; \mathbb{C}), \qquad G_{\delta,n}\varphi = \boldsymbol{e}_3 \cdot \boldsymbol{H}^s|_{\mathcal{M}}.$$

In the following, we refer to this measurement setup as normal excitations and measurements, and to the corresponding measurement data as *normal measurement data*.

Note that these normal measurement data can be viewed as a Galerkin projection of the full 3D measurement operator G_δ considered in [19, (3.7)], i.e.,

$$G_{\delta,n}\varphi = \boldsymbol{e}_3 \cdot G_\delta(\varphi \boldsymbol{e}_3).$$

As such the asymptotic expansion of the normal measurement data as $\delta \to 0$ (i.e., as the scatterers $D_{\delta,l}$ shrink to the points $\boldsymbol{z}_l$, $l = 1, \ldots, p$) follows readily from [19, (3.7)].

Theorem 2.1. *Assume that $\varphi \in L^2(\mathcal{M}; \mathbb{C})$ and let $\boldsymbol{H}^i$ be the corresponding incident field from (3). Then there exist symmetric and positive-definite matrices $\mathbb{M}^0_{B_1}, \ldots, \mathbb{M}^0_{B_p} \in \mathbb{R}^{3\times 3}$ and $\mathbb{M}^\infty_{B_1}, \ldots, \mathbb{M}^\infty_{B_p} \in \mathbb{R}^{3\times 3}$, called magnetic and electric polarizability tensors corresponding to $B_1, \ldots, B_p$, respectively, such that*

$$\left\| G_{\delta,n}\varphi - \delta^3 \sum_{l=1}^{p} \boldsymbol{e}_3 \cdot \left(-k_-^2 \mathbb{G}^m(\cdot, \boldsymbol{z}_l)\mathbb{M}^0_{B_l} \boldsymbol{H}^i(\boldsymbol{z}_l) + \frac{\mu_-}{\mu_+} \mathbf{curl}_x\, \mathbb{G}^e(\cdot, \boldsymbol{z}_l)\, \mathbb{M}^\infty_{B_l} \mathbf{curl}\, \boldsymbol{H}^i(\boldsymbol{z}_l) \right) \right\|_{L^2(\mathcal{M};\mathbb{C})} \leqslant C\delta^4 \|\varphi\|_{L^2(\mathcal{M};\mathbb{C})}, \tag{4}$$

as $\delta \to 0$, where the constant $C > 0$ is independent of δ and φ.

As usual, in (4) vector operators operate on matrices column by column.

3. Characterization of the scatterers in terms of normal measurement data

We are now going to use the asymptotic expansion (4) to characterize the positions of the scatterers in terms of normal measurement data. While this goal is similar to the one in [19], we emphasize that the proofs from [19], which rely on unique continuation results for solutions of boundary and transmission problems for Maxwell's equations, do not apply here. Rather, we have to use a different approach, which is based on the scalar Helmholtz equation for the vertical component of the magnetic field.

To begin with, we define the operator $T_n : L^2(\mathcal{M}; \mathbb{C}) \to L^2(\mathcal{M}; \mathbb{C})$,

$$T_n\varphi = \sum_{l=1}^{p} \boldsymbol{e}_3 \cdot \left(-k_-^2 \mathbb{G}^m(\cdot, \boldsymbol{z}_l)\mathbb{M}^0_{B_l} \boldsymbol{H}^i(\boldsymbol{z}_l) + \frac{\mu_-}{\mu_+} \mathbf{curl}_x\, \mathbb{G}^e(\cdot, \boldsymbol{z}_l)\, \mathbb{M}^\infty_{B_l} \mathbf{curl}\, \boldsymbol{H}^i(\boldsymbol{z}_l) \right),$$

by the leading order term of the asymptotic expansion (4). This operator can be factorized in the form $T_n = R_n M R_n^\top$, where $R_n : \mathbb{C}^{3\times 2p} \to L^2(\mathcal{M}; \mathbb{C})$ is defined by

$$R_n \boldsymbol{a} = k_-^2 \sum_{l=1}^{p} \boldsymbol{e}_3 \cdot \left(\mathbb{G}^m(\cdot, \boldsymbol{z}_l)\boldsymbol{a}_l + \frac{\mu_-}{\mu_+} \mathbf{curl}_x \mathbb{G}^e(\cdot, \boldsymbol{z}_l)\boldsymbol{a}_{p+l} \right), \tag{5}$$

for $\boldsymbol{a} = (\boldsymbol{a}_1, \ldots, \boldsymbol{a}_{2p}) \in \mathbb{C}^{3\times 2p}$, $\boldsymbol{a}_l \in \mathbb{C}^3$, and $M : \mathbb{C}^{3\times 2p} \to \mathbb{C}^{3\times 2p}$ is defined by

$$M\boldsymbol{a} = \frac{\mu_+}{\mu_-}\left(-\mathbb{M}^0_{B_1}\boldsymbol{a}_1, \ldots, -\mathbb{M}^0_{B_p}\boldsymbol{a}_p, \frac{1}{k_-^2}\mathbb{M}^\infty_{B_1}\boldsymbol{a}_{p+1}, \ldots, \frac{1}{k_-^2}\mathbb{M}^\infty_{B_p}\boldsymbol{a}_{2p}\right).$$

A short calculation shows that $R_n^\top : L^2(\mathcal{M}; \mathbb{C}) \to \mathbb{C}^{3\times 2p}$ is given by

$$R_n^\top \varphi = \frac{\mu_-}{\mu_+}(\boldsymbol{H}^i(\boldsymbol{z}_1), \ldots, \boldsymbol{H}^i(\boldsymbol{z}_p), \mathbf{curl}\,\boldsymbol{H}^i(\boldsymbol{z}_1), \ldots, \mathbf{curl}\,\boldsymbol{H}^i(\boldsymbol{z}_p)),$$

where $\boldsymbol{H}^i$ is the incident magnetic field from (3) (so far, this is similar to [19, section 9]). Note that the operator T_n corresponds to the multi-static response matrix considered in [21], and which has been decomposed analogously in that work.

One major difference to [19] is the lack of injectivity of the operator R_n.

Lemma 3.1. *The operator R_n has a non-trivial null space given by*

$$\mathcal{N}(R_n) = \{\mathbf{0}\}^p \times (\mathbb{C}\boldsymbol{e}_3)^p := \{(\mathbf{0}, \ldots, \mathbf{0}, t_1\boldsymbol{e}_3, \ldots, t_p\boldsymbol{e}_3) \mid t_1, \ldots, t_p \in \mathbb{C}\}.$$

Proof. Let $\boldsymbol{a} \in \mathcal{N}(R_n)$. Then,

$$\tilde{\boldsymbol{H}} := k_-^2 \sum_{l=1}^{p}\left(\mathbb{G}^m(\cdot, \boldsymbol{z}_l)\boldsymbol{a}_l + \frac{\mu_-}{\mu}\,\mathbf{curl}_x\mathbb{G}^e(\cdot, \boldsymbol{z}_l)\,\boldsymbol{a}_{p+l}\right)$$

together with the corresponding electric field $\tilde{\boldsymbol{E}} := -\frac{1}{\mathrm{i}\omega\varepsilon}\,\mathbf{curl}\,\tilde{\boldsymbol{H}}$ fulfils Maxwell's equations (1) in $\mathbb{R}^3\setminus\bigcup_{l=1}^p\{\boldsymbol{z}_l\}$ and the radiation condition (2), and its normal component vanishes on $\mathcal{M}$, i.e. $\boldsymbol{e}_3\cdot\tilde{\boldsymbol{H}}|_{\mathcal{M}} = 0$. Since $\boldsymbol{e}_3\cdot\tilde{\boldsymbol{H}}|_{\Sigma_d}$ is analytic, it has to vanish on Σ_d, and therefore, $\tilde{H}_3 := \boldsymbol{e}_3\cdot\tilde{\boldsymbol{H}}$ is a radiating solution of Helmholtz's equation $\Delta\tilde{H}_3 + k_+^2\tilde{H}_3 = 0$ in the half space $\{\boldsymbol{x} \in \mathbb{R}^3 \mid \boldsymbol{x}\cdot\boldsymbol{e}_3 > d\}$ with $\tilde{H}_3|_{\Sigma_d} = 0$. Applying the reflection principle $\tilde{H}_3$ can be extended to $\mathbb{R}^3$ by

$$\tilde{H}_3^e(\boldsymbol{x}) := \begin{cases}\tilde{H}_3(\boldsymbol{x}), & \boldsymbol{x}\cdot\boldsymbol{e}_3 \geqslant d,\\ -\tilde{H}_3(\alpha(\boldsymbol{x})), & \boldsymbol{x}\cdot\boldsymbol{e}_3 < d,\end{cases}$$

where α denotes a reflection operator given by $\alpha : \mathbb{R}^3 \to \mathbb{R}^3$, $\alpha(\boldsymbol{x}) := \boldsymbol{x} - 2(\boldsymbol{x}\cdot\boldsymbol{e}_3 - d)\boldsymbol{e}_3$. By construction $\tilde{H}_3^e$ and $\partial\tilde{H}_3/\partial\boldsymbol{e}_3$ are continuous across Σ_d and $\tilde{H}_3^e$ satisfies the Sommerfeld radiation condition. Hence $\tilde{H}_3^e$ is a radiating solution of Helmholtz's equation $\Delta\tilde{H}_3^e + k_+^2\tilde{H}_3^e = 0$ in $\mathbb{R}^3$. Thus (cf [13, p 20]), $\tilde{H}_3^e = 0$ in $\mathbb{R}^3$, especially $\tilde{H}_3 = 0$ in $\{\boldsymbol{x} \in \mathbb{R}^3 \mid \boldsymbol{x}\cdot\boldsymbol{e}_3 > d\}$. By analyticity $\tilde{H}_3 = 0$ in $\mathbb{R}^3_+$, and since $[\mu\tilde{H}_3]_{\Sigma_0} = 0$ and $[\partial\tilde{H}_3/\partial\boldsymbol{e}_3]_{\Sigma_0} = 0$ (cf [14, p 439]), Holmgren's theorem (cf [25, theorem 2.2, p 41]) yields that $\tilde{H}_3 = 0$ in a neighborhood of Σ_0 in $\mathbb{R}^3_-$. Once more using analyticity we conclude that $\tilde{H}_3 = 0$ in $\mathbb{R}^3\setminus\bigcup_{l=1}^p\{\boldsymbol{z}_l\}$.

Studying $\tilde{H}_3$ close to $\boldsymbol{z}_l$, $1 \leqslant l \leqslant p$, we find that $\lim_{t\to 0}\tilde{H}_3(\boldsymbol{z}_l + t\boldsymbol{b}) = 0$ for any $\boldsymbol{b} \in \mathbb{R}^3$. Observing that $\mathbb{G}^m(\cdot, \boldsymbol{z}_l)$ and $\mathbb{G}^e(\cdot, \boldsymbol{z}_l)$ are smooth perturbations of the dyadic Green's function for the homogeneous background medium with wave number k_- around $\boldsymbol{z}_l$, we find that the singularity of $\mathbb{G}^m(\cdot, \boldsymbol{z}_l)$ in $\boldsymbol{z}_l$ is of order 3, while the singularity of $\mathbf{curl}_x\mathbb{G}^e(\cdot, \boldsymbol{z}_l)$ in $\boldsymbol{z}_l$ is only of order 2 (cf [18, pp 125–126] for details). More precisely, we have

$$\begin{aligned}
&\boldsymbol{e}_3\cdot\mathbb{G}^m(\boldsymbol{z}_l + t\,\boldsymbol{e}_3, \boldsymbol{z}_l)\,\boldsymbol{a}_l = t^{-3}c_1(-2\,\boldsymbol{a}_l\cdot\boldsymbol{e}_3) + \mathcal{O}(t^{-2}),\\
&\boldsymbol{e}_3\cdot\mathbb{G}^m(\boldsymbol{z}_l + t(\boldsymbol{e}_1 + \boldsymbol{e}_3), \boldsymbol{z}_l)\,\boldsymbol{a}_l = t^{-3}c_2(-3\,\boldsymbol{a}_l\cdot\boldsymbol{e}_1 - \boldsymbol{a}_l\cdot\boldsymbol{e}_3) + \mathcal{O}(t^{-2}),\\
&\boldsymbol{e}_3\cdot\mathbb{G}^m(\boldsymbol{z}_l + t(\boldsymbol{e}_2 + \boldsymbol{e}_3), \boldsymbol{z}_l)\,\boldsymbol{a}_l = t^{-3}c_2(-3\,\boldsymbol{a}_l\cdot\boldsymbol{e}_2 - \boldsymbol{a}_l\cdot\boldsymbol{e}_3) + \mathcal{O}(t^{-2})
\end{aligned}$$

as $t \to 0$, where c_1 and c_2 are constants, and therefore $\boldsymbol{a}_l = \mathbf{0}$. Furthermore,

$$\begin{aligned}
&\boldsymbol{e}_3\cdot\mathbf{curl}_x\mathbb{G}^e(\boldsymbol{z}_l + t\,\boldsymbol{e}_1, \boldsymbol{z}_l)\,\boldsymbol{a}_{p+l} = t^{-2}c_3\,\boldsymbol{a}_{p+l}\cdot\boldsymbol{e}_2 + \mathcal{O}(t^{-1}),\\
&\boldsymbol{e}_3\cdot\mathbf{curl}_x\mathbb{G}^e(\boldsymbol{z}_l + t\,\boldsymbol{e}_2, \boldsymbol{z}_l)\,\boldsymbol{a}_{p+l} = t^{-2}c_3(-\boldsymbol{a}_{p+l}\cdot\boldsymbol{e}_1) + \mathcal{O}(t^{-1})
\end{aligned}$$

as $t \to 0$, where c_3 is a constant, and thus $\boldsymbol{a}_{p+l}$ is a multiple of $\boldsymbol{e}_3$. Hence, $\mathcal{N}(R_n) \subset \{\boldsymbol{0}\}^p \times (\mathbb{C}\,\boldsymbol{e}_3)^p$.

On the other hand, $\boldsymbol{e}_3 \cdot \left(\frac{1}{\mu}\mathbf{curl}_x\, \mathbb{G}^e(\cdot, \boldsymbol{z}_l)\, \boldsymbol{e}_3\right)$ is bounded in a neighborhood of $\boldsymbol{z}_l$ (see [18, p 125]), and therefore an entire solution of a transmission problem for Helmholtz's equation satisfying the Sommerfeld radiation condition. Hence, $\boldsymbol{e}_3 \cdot \left(\frac{1}{\mu}\,\mathbf{curl}_x\, \mathbb{G}^e(\cdot, \boldsymbol{z}_l)\, \boldsymbol{e}_3\right) = 0$ (cf [26] if $k \in \mathbb{R}$, and [28, proposition 2.3] if $k \notin \mathbb{R}$), and we obtain that $\{\boldsymbol{0}\}^p \times (\mathbb{C}\,\boldsymbol{e}_3)^p \subset \mathcal{N}(R_n)$. □

The non-injectivity of R_n distinguishes normal measurement data from fully three-dimensional measurement data (or tangential data), and has fundamental consequences on MUSIC reconstruction methods, because the dimension of the essential range of the measurement operator $G_{\delta,n}$ changes.

Proposition 3.1. *The range of T_n has dimension $5p$ and is given by*

$$\mathcal{R}(T_n) = \operatorname{spann}_{\mathbb{C}}\{\boldsymbol{e}_3 \cdot \mathbb{G}^m(\cdot, \boldsymbol{z}_l)\boldsymbol{e}_{j_1},\, \boldsymbol{e}_3 \cdot \mathbf{curl}_x \mathbb{G}^e(\cdot, \boldsymbol{z}_l)\boldsymbol{e}_{j_2} \\ |j_1 = 1, 2, 3;\, j_2 = 1, 2;\, l = 1, \ldots, p\}.$$

Proof. Since $\mathcal{R}(R_n)$ is finite dimensional and M is symmetric, we find that

$$\mathcal{R}(R_n) = \mathcal{N}\big(R_n^\top\big)^a \qquad \text{and} \qquad \mathcal{R}\big(R_n M R_n^\top\big) = \mathcal{N}\big(R_n M R_n^\top\big)^a, \tag{6}$$

where $\mathcal{N}\big(R_n^\top\big)^a$ and $\mathcal{N}\big(R_n M R_n^\top\big)^a$ denote the annihilators of $\mathcal{N}\big(R_n^\top\big)$ and $\mathcal{N}\big(R_n M R_n^\top\big)$, respectively, in $L^2(\mathcal{M}; \mathbb{C})$. Furthermore, for $\phi \in \mathcal{N}\big(R_n M R_n^\top\big)$ we have

$$0 = \big\langle \phi,\, R_n M R_n^\top \phi \big\rangle_{\mathcal{M}} = \big\langle R_n^\top \phi,\, M R_n^\top \phi \big\rangle_{\mathbb{C}^{3\times 2p}},$$

and hence we can use the positive definiteness of the electric and magnetic polarizability tensors to conclude that $\phi \in \mathcal{N}\big(R_n^\top\big)$. It follows that $\mathcal{N}\big(R_n M R_n^\top\big) \subset \mathcal{N}\big(R_n^\top\big)$, and therefore we have $\mathcal{R}(R_n) \subset \mathcal{R}\big(R_n M R_n^\top\big)$ according to (6). Thus we have shown that $\mathcal{R}(R_n) = \mathcal{R}(T_n)$, and the assertion is now a consequence of (5) and lemma 3.1. □

For the implementation of a MUSIC algorithm it is essential to characterize the range of T_n in terms of the positions of the infinitesimal scatterers. In [19], it has been shown that for full 3D measurements (and the same applies for tangential data, too) the trace of the magnetic field of a (magnetic or electric) dipole on $\mathcal{M}$ belongs to the range of the leading order term of the asymptotic expansion of the corresponding measurement operator, if and only if the location of the dipole coincides with the position of any one of the scatterers. As indicated by proposition 3.1 the situation is slightly more delicate for normal measurement data:

Proposition 3.2. *Let $\boldsymbol{d} = (\boldsymbol{d}_1, \boldsymbol{d}_2) \in (\mathbb{C}^3 \times \mathbb{C}^3)\backslash(\{\boldsymbol{0}\} \times (\mathbb{C}\boldsymbol{e}_3))$, $\boldsymbol{y} \in \mathbb{R}^3_-$ and*

$$g^n_{y,d} := \boldsymbol{e}_3 \cdot (\mathbb{G}^m(\cdot, \boldsymbol{y})\, \boldsymbol{d}_1 + \mathbf{curl}_x\, \mathbb{G}^e(\cdot, \boldsymbol{y})\, \boldsymbol{d}_2)|_{\mathcal{M}}. \tag{7}$$

Then, $g^n_{y,d} \in \mathcal{R}(T_n)$ if and only if $\boldsymbol{y} \in \{\boldsymbol{z}_1, \ldots, \boldsymbol{z}_p\}$.

Proof. If $g^n_{y,d} \in \mathcal{R}(T_n)$ then we can write $g^n_{y,d}$ as

$$g^n_{y,d} = \sum_{l=1}^{p} (\boldsymbol{e}_3 \cdot \mathbb{G}^m(\cdot, \boldsymbol{z}_l)\boldsymbol{a}_l + \boldsymbol{e}_3 \cdot \mathbf{curl}_x\, \mathbb{G}^e(\cdot, \boldsymbol{z}_l)\, \boldsymbol{a}_{l+p})) \qquad \text{on} \quad \mathcal{M},$$

with $\boldsymbol{a}_1, \ldots, \boldsymbol{a}_p \in \mathbb{C}^3$ and $\boldsymbol{a}_{p+1}, \ldots, \boldsymbol{a}_{2p} \in \mathbb{C}^3\backslash(\mathbb{C}\boldsymbol{e}_3)$ according to proposition 3.1. Moreover,

$$\boldsymbol{H}^a := \sum_{l=1}^{p} \left(\mathbb{G}^m(\cdot, \boldsymbol{z}_l)\boldsymbol{a}_l + \frac{\mu_+}{\mu}\, \mathbf{curl}_x \mathbb{G}^e(\cdot, \boldsymbol{z}_l)\boldsymbol{a}_{l+p}\right)$$

as well as

$$\boldsymbol{H}^d := \mathbb{G}^m(\cdot, \boldsymbol{y})\, \boldsymbol{d}_1 + \frac{\mu_+}{\mu}\, \mathbf{curl}_x\, \mathbb{G}^e(\cdot, \boldsymbol{y})\, \boldsymbol{d}_2$$

together with the corresponding electric fields fulfil Maxwell's equations (1) in $\mathbb{R}^3 \setminus \big(\bigcup_{l=1}^p \{\boldsymbol{z}_l\} \cup \{\boldsymbol{y}\} \big)$ and the radiation condition (2). Since their normal components coincide on $\mathcal{M}$, $\tilde{\boldsymbol{H}} := \boldsymbol{H}^a - \boldsymbol{H}^d$ together with the associated electric field $\tilde{\boldsymbol{E}}$ is a radiating solution of (1) in $\mathbb{R}^3 \setminus \big(\bigcup_{l=1}^p \{\boldsymbol{z}_l\} \cup \{\boldsymbol{y}\} \big)$ with vanishing normal component on $\mathcal{M}$, i.e. $\boldsymbol{e}_3 \cdot \tilde{\boldsymbol{H}}|_{\mathcal{M}} = 0$. As in the proof of lemma 3.1 we conclude that $\tilde{H}_3 = 0$ in $\mathbb{R}^3 \setminus \big(\bigcup_{l=1}^p \{\boldsymbol{z}_l\} \cup \{\boldsymbol{y}\} \big)$, which means that $H_3^a = H_3^d$ in $\mathbb{R}^3 \setminus \big(\bigcup_{l=1}^p \{\boldsymbol{z}_l\} \cup \{\boldsymbol{y}\} \big)$. However, this implies that $\boldsymbol{y} \in \{\boldsymbol{z}_1, \ldots, \boldsymbol{z}_p\}$, which shows the necessity of this condition. Its sufficiency is a consequence of proposition 3.1. □

In other words, the so-called test dipoles $g_{y,d}^n$ to be used in the MUSIC algorithm must not correspond to electric dipoles with a vertical polarization. Note that, in contrast to [19], the magnetic field $\tilde{\boldsymbol{H}}$ constructed in the proof of proposition 3.2 is not vanishing in general—only its vertical component is.

4. The MUSIC reconstruction method

To implement the range characterization from proposition 3.2 in a MUSIC algorithm, we employ a three-dimensional grid of test points $\boldsymbol{y} \in \mathbb{R}^3_-$ in some region of interest contained in the lower half space, and consider test dipoles $g_{y,d}^n$ as in proposition 3.2.

As the operator T_n has finite rank, we can define the orthogonal projection $P : L^2(\mathcal{M}; \mathbb{C}) \to \mathcal{R}(T_n)$ on the range of T_n, with which the angle $\beta(\boldsymbol{y})$ between $g_{y,d}^n$ and $\mathcal{R}(T_n)$ is given by

$$\cot \beta(\boldsymbol{y}) = \frac{\big\| P g_{y,d}^n \big\|_{L^2(\mathcal{M};\mathbb{C})}}{\big\| (I - P) g_{y,d}^n \big\|_{L^2(\mathcal{M};\mathbb{C})}}, \qquad \boldsymbol{y} \in \mathbb{R}^3_-,$$

where I denotes the identity operator. Then proposition 3.2 yields that

$$\boldsymbol{y} \in \{\boldsymbol{z}_1, \ldots, \boldsymbol{z}_p\} \quad \Longleftrightarrow \quad \beta(\boldsymbol{y}) = 0 \quad \Longleftrightarrow \quad \cot \beta(\boldsymbol{y}) = \infty. \tag{8}$$

As

$$T_n = \frac{1}{\delta^3} G_{\delta,n} + O(\delta)$$

by theorem 2.1, we can approximate the projection P by the projection

$$P_{5p}^\delta : L^2(\mathcal{M}; \mathbb{C}) \to \operatorname{spann}_{\mathbb{C}} \big\{ \boldsymbol{u}_1^\delta, \ldots, \boldsymbol{u}_{5p}^\delta \big\}$$

on the essential range of $G_{\delta,n}$, i.e., our normal measurement data, which is spanned by the left singular vectors $\boldsymbol{u}_1^\delta, \ldots, \boldsymbol{u}_{5p}^\delta$ of the $5p$ largest singular values of $G_{\delta,n}$. Therewith, we approximate

$$\cot \beta(\boldsymbol{y}) \approx \frac{\big\| P_{5p}^\delta g_{y,d}^n \big\|_{L^2(\mathcal{M};\mathbb{C})}}{\big\| (I - P_{5p}^\delta) g_{y,d}^n \big\|_{L^2(\mathcal{M};\mathbb{C})}} =: \cot \beta_{5p}^\delta(\boldsymbol{y}). \tag{9}$$

In view of (8), $\cot \beta_{5p}^\delta(\boldsymbol{y})$ should be large for test points $\boldsymbol{y}$ which are close to the points $\boldsymbol{z}_1, \ldots, \boldsymbol{z}_p$, and hence, the positions of the scatterers can be visualized, for example, by plotting $\cot \beta_{5p}^\delta$ or isosurfaces of this indicator function in the region of interest.

Following [9], the unknown number of scatterers $p \in \mathbb{N}$ could be found by estimating the dimension of the essential range of G_δ, which amounts to searching for a reasonable gap in the set of singular values. However, in our numerical tests we found that this approach only

works well if the scatterers are very small compared to (i) the distances between each other and (ii) their distance to the interface. Furthermore, the signal-to-noise ratio must not be too small. A more stable way to estimate p is to visualize $\cot \beta_l^\delta$ from (9) for increasing values $l = 5, 10, 15, 20, \ldots$. Typically, the number of reconstructed scatterers increases with l until all scatterers have been found. We refer to [9, 20] for numerical tests of these strategies.

We illustrate the MUSIC algorithm with normal measurement data by means of some numerical examples, and we compare the reconstructions to those in [19, 20] obtained from fully three-dimensional excitations and measurements. As in [19, 20] we therefore consider a two-layered background medium, where $\varepsilon_+ = \varepsilon_0 = 8.85 \times 10^{-12}\,\mathrm{Fm}^{-1}$ and $\mu_+ = \mu_0 = 8.85 \times 10^{-12}\,\mathrm{Hm}^{-1}$, and

$$\varepsilon_- = \varepsilon_0\left(\varepsilon_r + \mathrm{i}\,\frac{\sigma}{\omega\varepsilon_0}\right) = (0.867 + \mathrm{i}\,59.5) \times 10^{-10}\,\mathrm{Fm}^{-1},$$
$$\mu_- = (1+\chi)\mu_0 = 1.26 \times 10^{-6}\,\mathrm{Hm}^{-1},$$

modeling air and soil, respectively. The particular parameters $\sigma = 7.5 \times 10^{-4}\,\mathrm{Sm}^{-1}$, $\chi = 1.9 \times 10^{-5}$, and $\varepsilon_r = 9.8$, which we use for the lower half space refer to measurement data for a poor clay sand (cf [22]).

The measurement device in this example operates on a square $\mathcal{M}$ of size $50 \times 50\ \mathrm{cm}^2$ parallel to the surface of ground with its center 10 cm above the origin $(0, 0, 0)$. Modeling a device of 36 coils we impose vertically polarized magnetic dipoles with a frequency of 20 kHz on a 6×6 equidistant grid on $\mathcal{M}$, simulate the vertical components of the resulting scattered fields, and evaluate these fields on the same grid, using a Nyström's method for two-layered background media. This yields a 36×36 matrix $G^h_{\delta,n}$ approximating the measurement operator $G_{\delta,n}$. The wave numbers in this example are $k_+ = 4.22 \times 10^{-4}\ \mathrm{m}^{-1}$ in air and $k_- = (7.77 + \mathrm{i}\,7.66) \times 10^{-3}\ \mathrm{m}^{-1}$ in soil, which corresponds to wave lengths $\lambda_+ = 14.9$ km and $\lambda_- = 0.81$ km.

As a test case, two perfectly conducting ellipsoidal obstacles with semi-axes of length $(2, 2, 0.5)$ cm and $(2, 1, 4)$ cm, respectively, are assumed to be buried in the lower half space. The centers of the two scatterers are located at $(10, -15, -10)$ cm and $(-15, 10, -30)$ cm, respectively. Observe that the scattering objects are smaller than the wavelengths in both half spaces by many orders of magnitude. Our simulated forward data contain an estimated numerical error of 1.1%, and additionally we add 3% uniformly distributed error to simulate measurement errors (noise).

In the MUSIC reconstruction method we use the test function $g^n_{y,d}$ from (7) with polarization vector $\boldsymbol{d} = (\boldsymbol{e}_3, \boldsymbol{0})$. Its numerical implementation is the same that has been used in [19, 20]. We compute the singular value decomposition of the matrix $G^h_{\delta,n}$, and use the left singular vectors to approximate the indicator function $\cot \beta^\delta_{10}$ from (9) on a three-dimensional equidistant grid with step size 0.5 cm in the region of interest $[-25, 25]^2 \times [-40, 0]\ \mathrm{cm}^3$ in the lower half space.

Figure 1 shows cross-sectional plots of $\cot \beta^\delta_{10}(\boldsymbol{y})$ at $y_3 = -10$ and $y_3 = -30$ cm, respectively. According to proposition 3.2 the local maxima of $\cot \beta^\delta_{10}$ indicate the approximate positions of the scatterers, but the values of these local maxima are not necessarily the same for each scatterer; they rather depend on the quality of the approximation in (9), and therefore on the size and position of the scatterers itself, but also on the noise level.

The left-hand plot in figure 2 shows isosurface plots of $\cot \beta^\delta_{10}$ and their projections on the coordinate planes. This yields a three-dimensional visualization which provides a certain impression on the approximate positions of buried objects. The smaller these isosurfaces are, the better the positions of the scatterers can be estimated from such plots. On the other hand, the threshold cannot be too large, as the isosurfaces should not degenerate to a point, or even

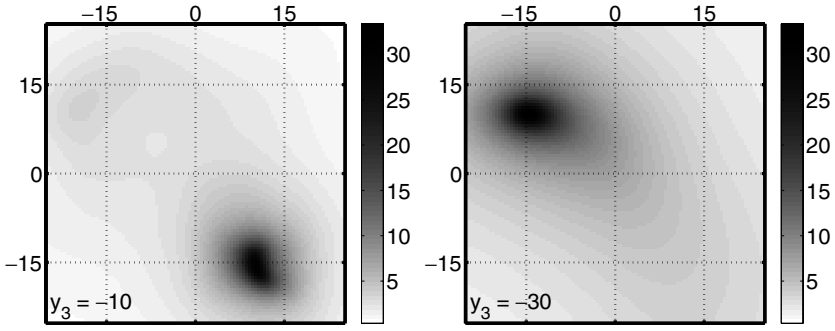

Figure 1. Cross-sectional plots of cot $\beta_{10}^{\delta}(\boldsymbol{y})$ at $y_3 = -10$ cm (left) and $y_3 = -30$ cm (right).

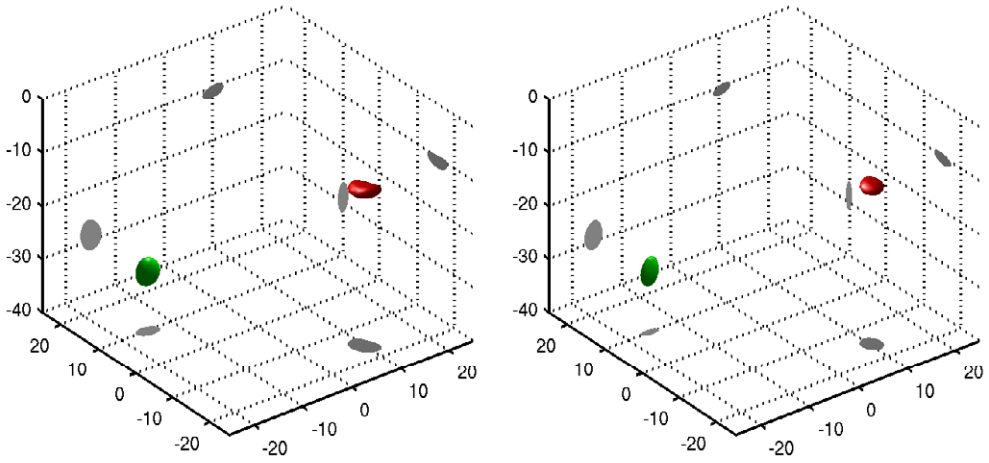

Figure 2. Reconstruction from normal measurement data (left) versus reconstruction from full three-dimensional measurement data (right).

an empty set, to be clearly visible. Also, as we have argued before, a reasonable threshold value will vary with each individual scatterer. We therefore use different thresholds in different areas of the region of interest, and we determine the corresponding values for cot β_{10}^{δ} from a visual inspection of several cross-sectional plots with different heights y_3 as in figure 1. Here, the isosurface corresponding to the upper obstacle uses the threshold cot $\beta_{10}^{\delta} = 30$, while the other one corresponds to cot $\beta_{10}^{\delta} = 35$. It should be possible to develop an automatical routine for finding reasonable thresholds, but this is beyond the scope of this paper.

For comparison the right-hand plot in figure 2 shows reconstructions obtained from fully three-dimensional excitations and measurements as discussed in [19, 20]. Here the forward data are computed by the same Nyström method as before, containing 3.4% estimated relative numerical error and additional 3% uniformly distributed data noise. The isosurface corresponding to the upper obstacle is given by cot $\tilde{\beta}_{12}^{\delta} = 45$ and the other one corresponds to cot $\tilde{\beta}_{12}^{\delta} = 55$. The angle $\tilde{\beta}_{12}^{\delta}$ is defined similar to (9), but instead of the left singular vectors of $G_{\delta,n}^{h}$ the left singular vectors of the measurement operator corresponding to the three-dimensional excitation and measurement data are used, and the test function $g_{y,d}^{n}$ is replaced by $\boldsymbol{g}_{y,d} := (\mathbb{G}^m(\cdot, \boldsymbol{y})\, \boldsymbol{d}_1 + \mathbf{curl}_y \mathbb{G}^e(\cdot, \boldsymbol{y})\, \boldsymbol{d}_2)|_{\mathcal{M}}$ with $\boldsymbol{d}_1 = \boldsymbol{e}_3$ and $\boldsymbol{d}_2 = \mathbf{0}$. As both,

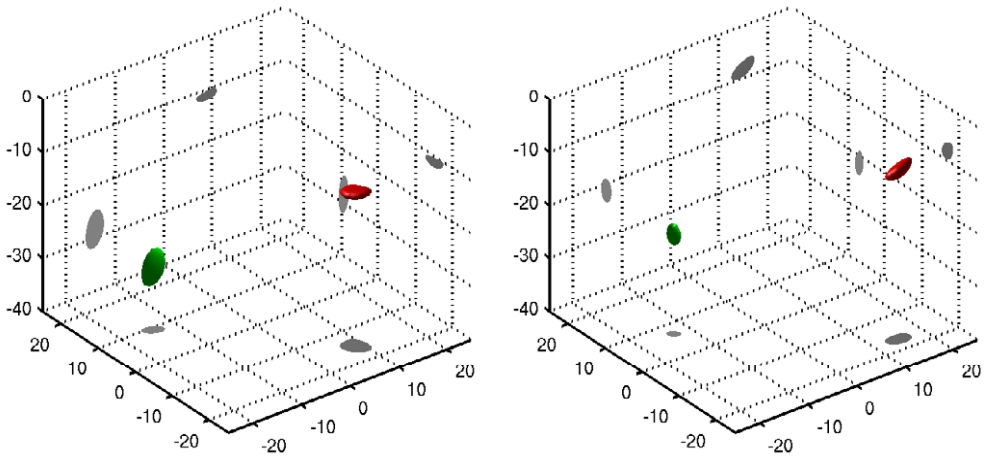

Figure 3. Reconstruction from normal measurement data with 10% noise (left) and 25% noise (right).

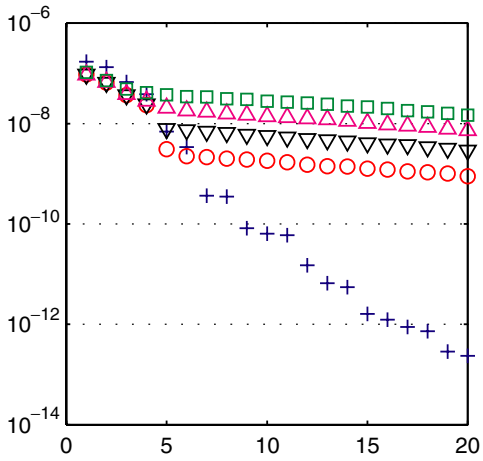

Figure 4. Singular values of the measurement operators $G^h_{\delta,n}$ (+ without additional noise, ○ with 3% noise, ▽ with 10% noise, △ with 25% noise, □ with 50% noise).

the test functions and the measurement data are different in the two setups, it is no surprise that the thresholds chosen in the two subplots of figure 2 are different as well.

For both settings the MUSIC algorithm detects the two scatterers at about the correct location; even the shape of the isosurfaces nicely agrees with the general shape of the scatterers, although this is not supported by our theory. The two reconstructions are of comparable quality, but the method presented here uses only one-ninth of the data used by the original method from [19, 20].

In an attempt to study the effect of noise on our algorithm, we show in figure 3 two reconstructions for the same forward problem as above (normal measurement data only), but based on data that have been perturbed by 10% and 25% additive noise, respectively. With 10% noise the positions of the scatterers are still relatively well reconstructed, whereas with 25% noise the position of the lower object has been misplaced by about 10 cm. Still, these are

excellent results which do benefit to some extent from the fact that the signals from the two scatterers within the data have approximately equal strength.

When we increase the noise level even further, then the reconstructions show only one object located closely to the center of mass of the union of the two scatterers. This is due to the fact that then only three singular values of $G^h_{\delta,n}$ stick out of the noise level (cf figure 4), and the corresponding singular vectors contain too little information to distinguish the two scatterers.

For a more detailed study of the resolution and the robustness of MUSIC methods for electromagnetic subsurface exploration we refer to [20].

5. Conclusions

Our theoretical results show that the MUSIC algorithm can be used to detect small objects from time-harmonic electromagnetic scattering data using normal excitations and measurements only. We have exemplified that the reconstructed positions of the scatterers are comparable to those obtained from full three-dimensional excitations and measurements. We have also seen that in practice the applicability will ultimately depend on the accuracy with which the scattered field can be measured.

Acknowledgments

The authors are grateful to Roland Potthast and his group for providing their codes from [15] to generate the forward data for the numerical examples, and to Christoph Schneider for his code for the linear sampling method from [17], which has been adapted to implement the MUSIC reconstruction method presented here. We are also pleased to thank Habib Ammari for his support and for many interesting discussions in the course of this project.

References

[1] Ammari H, Griesmaier R and Hanke M 2007 Identification of small inhomogeneities: asymptotic factorization *Math. Comput.* **76** 1425–48

[2] Ammari H, Iakovleva E and Kang H 2005 Reconstruction of a small inclusion in a two-dimensional open waveguide *SIAM J. Appl. Math.* **65** 2107–27

[3] Ammari H, Iakovleva E and Lesselier D 2005 Two numerical methods for recovering small electromagnetic inclusions from scattering amplitude at a fixed frequency *SIAM J. Sci. Comput.* **27** 130–58

[4] Ammari H, Iakovleva E and Lesselier D 2005 A MUSIC algorithm for locating small inclusions buried in a half–space from the scattering amplitude at a fixed frequency *Multiscale Model. Simul.* **3** 597–628

[5] Ammari H, Iakovleva E, Lesselier D and Perrusson G 2007 MUSIC-type electromagnetic imaging of a collection of small threedimensional bounded inclusions *SIAM J. Sci. Comput.* **29** 674–709

[6] Ammari H and Kang H 2004 *Reconstruction of Small Inhomogeneities from Boundary Measurements* (*Lecture Notes in Math.* vol 1846) (Berlin: Springer)

[7] Ammari H and Kang H 2007 *Polarization and Moment Tensors with Applications to Inverse Problems and Effective Medium Theory* (*Appl. Math. Sci.* vol 162) (Berlin: Springer)

[8] Arens T, Lechleiter A and Luke D A MUSIC for extended scatterers as an instance of the factorization method *SIAM J. Appl. Math.* at press

[9] Brühl M, Hanke M and Vogelius M S 2003 A direct impedance tomography algorithm for locating small inhomogeneities *Numer. Math.* **93** 635–54

[10] Bruschini C 2000 Metal detectors in civil engineering and humanitarian demining: overview and tests of a commercial visualizing system *INSIGHT-Non-Destr. Test. Condition Monit.* **42** 89–97

[11] Cakoni F and Colton D 2006 *Qualitative Methods in Inverse Scattering Theory. An Introduction* (Interact. Mech. Math.) (Berlin: Springer)

[12] Cheney M 2001 The linear sampling method and the MUSIC algorithm *Inverse Problems* **17** 591–5

[13] Colton D and Kress R 1998 *Inverse Acoustic and Electromagnetic Scattering Theory* (*Appl. Math. Sci.* vol 93) 2nd edn (Berlin: Springer)
[14] Cutzach P–M and Hazard C 1998 Existence, uniqueness and analyticity properties for electromagnetic scattering in a two-layered medium *Math. Methods Appl. Sci.* **21** 433–61
[15] Delbary F, Erhard K, Kress R, Potthast R and Schulz J 2008 Inverse electromagnetic scattering in a two-layered medium with an application to mine detection *Inverse Problems* **24** 015002
[16] Devaney A J 1999 *Super-resolution Processing of Multi-static Data Using Time Reversal and MUSIC* (Boston, MA: Department of Electrical Engineering, Northeastern University) http://www.ece.neu.edu/faculty/devaney/ajd/preprints.htm
[17] Gebauer B, Hanke M, Kirsch A, Muniz W and Schneider C 2005 A sampling method for detecting buried objects using electromagnetic scattering *Inverse Problems* **21** 2035–50
[18] Griesmaier R 2008 *Detection of Small Buried Objects: Asymptotic Factorization and MUSIC, Johannes Gutenberg-Universität, Mainz, Dissertation* (http://nbn-resolving.de/urn/resolver.pl?urn=urn:nbn:de:hebis:77-16663)
[19] Griesmaier R 2008 An asymptotic factorization method for inverse electromagnetic scattering in layered media *SIAM J. Appl. Math.* **68** 1378–403
[20] Griesmaier R and Hanke M 2008 An asymptotic factorization method for inverse electromagnetic scattering in layered media: II. A numerical study http://www.math.udel.edu/ griesmai/publications/MUSICpartII.pdf
[21] Iakovleva E, Gdoura S, Lesselier D and Perrusson G 2007 Multistatic response matrix of a –3D inclusion in half space and MUSIC imaging *IEEE Trans. Antennas Propagat.* **55** 2598–609
[22] Igel J and Preetz H 2005 Elektromagnetische Bodenparameter und ihre Abhängigkeit von den Bodeneigenschaften. Zwischenbericht Projektverbund Humanitäres Minenräumen *Technical Report* Leibniz Institute of Applied Geosciences, Hannover
[23] Kirsch A 2002 The MUSIC algorithm and the factorization method in inverse scattering theory for inhomogeneous media *Inverse Problems* **18** 1025–40
[24] Kirsch A and Grinberg N 2008 *The Factorization Method for Inverse Problems* (*Oxford Lecture Ser. Math. Appl.* vol 36) (New York: Oxford University Press)
[25] Kress R 2002 Acoustic scattering: specific theoretical tools *Scattering. Scattering and Inverse Scattering in Pure and Applied Science* ed E R Pike and P C Sabatier (San Diego, CA: Academic) pp 37–51
[26] Kristensson G 1980 A uniqueness theorem for Helmholtz' equation: penetrable media with an infinite interface *SIAM J. Math. Anal.* **11** 1104–17
[27] Monk P 2003 *Finite Element Methods for Maxwell's Equations* (*Numer. Math. Sci. Comput.*) (New York: Oxford University Press)
[28] Petry M 1993 Über die Streuung zeitharmonischer Wellen im geschichteten Raum *Dissertation* Georg-August-Universität zu Göttingen, Göttingen